High temperature dielectric relaxation and impedance spectroscopy studies on BaBiO₃

Divyanshu Bhatnagar, Ratnamala Chatterjee*

Magnetics & Advanced Ceramics Laboratory, Physics Department, Indian Institute of Technology Delhi, New Delhi 110016, India

*Corresponding author. Tel.: (+91) 11-26596540/42; Email: rmala@physics.iitd.ac.in

ABSTRACT

BaBiO₃ (BBO) particles were successfully synthesized through solid-state route, to provide better understanding of its transport properties, which is not well studied yet. X-ray diffraction (XRD) measurement confirmed that the particles were crystallized with monoclinic structure in single phase. The Raman spectrum of BBO sample revealed the existence of two different Bi sites (the octahedral $BiO_{6/3}$ and the triangular pyramidal $BiO_{4/2}$ cluster). Subsequently, the observation of low resolution and lattice scale imaging through high resolution transmission electron microscope (HRTEM) indicated the formation of monoclinic BBO particles of size ~ 50-60 nm. The ring pattern obtained from selected area electron diffraction (SAED) inveterate polycrystalline nature of the sample and calculated structural parameters well harmonized with XRD results. As expected, BBO showed semiconducting behavior with resistivity of ~ 3.8 kΩ-cm at room temperature along with an excellent NTC (negative temperature coefficient) thermistor characteristic. The dielectric measurements and impedance spectroscopy studies reveal that BBO exhibit two typical characteristics, *i.e.*, diffuse phase transition and frequency dependent dielectric maxima, of relaxor oxides; with negative dielectric constant above 550 K. Copyright © 2016 VBRI Press.

Keywords: Rietveld refinement; Raman spectroscopy; electron microscopy; dielectric properties and impedance spectroscopy.

Introduction

Dielectric relaxor oxides with perovskite structure play a significant role in microelectronics and have numerous technological applications [**1, 2**]. Most of the relaxor perovskite materials (e.g., $Pb(Mg_{1/3}Nb_{2/3})O_3$ (PMN)] [**3**] $Pb(Zr,Ti)O_3$ (PZT) [**4**] and $Pb(Sc_{1/2}Nb_{1/2})O_3$ PSN [**5**]) useful for devices contain higher lead content that has major disadvantages due to ecological restriction and hazardous. Lead-free ceramics recently received considerable research attention to meet the above problem [**6-9**]. A lot of lead free perovskite ceramics such as $BaTiO_3$ [**10**], $Ba(ZrTi)O_3$ [**11**] $SrTiO_3$ [**12**], $BiFeO_3$ [**13**] and BBO [**14**] etc. have been investigated attributable to its not detrimental effect on environment, both in synthesis and its applications; as alternatives to the lead-rich ceramics. Study of various properties of these lead free perovskite ceramics would be very interesting from both physics and application point of view. This has attracted our attention to evaluate behavior of such non-lead system (BBO) in unexplored range.

Among lead free perovskites, Bismuth oxides are one of the most widely studied oxide materials as it possesses different properties like superconductivity, multiferroicity, photo-catalyst, high temperature electrolyte etc. [**15**]. In addition to other bismuth oxides, BBO has carved special interest among researchers as it undergoes a number of temperature-induced phase transitions associated with BiO_6 octahedral tilting [**16, 17**]. The monoclinic (P2₁/C) phase transforms into monoclinic (I2/m) at ~ 140 K in a continuous transformation which further converts into rhombohedral (R$\bar{3}$) structure at ~ 405 K through first order transition followed by a continuous transformation to cubic structure (Fm$\bar{3}$m) at ~ 725 K [**18**].

BBO crystallizes in distorted monoclinic perovskite structure [**19**], and this distortion is attributed to the coexistence of two valence states, Bi^{3+} $(6s^2)$ and Bi^{5+} $(6s^0)$ [**20**]. The resulting distortion contained an ordered alternation of Bi^{3+} and Bi^{5+} sites, and hence compound can be represented as $Ba_2Bi^{3+}Bi^{5+}O_6$ [**21**]. It has frozen breathing-type displacement of oxygen atoms around the Bi atoms combined with the tilting of the BiO_6 octahedral [**22**], which results in the semiconducting nature of BBO (p-type semiconductor with room temperature resistivity ~ 3.8 kΩ-cm) [**23**]. Moreover, in literature it has been shown that the semiconducting state is transformed to a superconducting state in $Ba_{1-x}K_xBiO_3$ (x ~ 0.35) [**24**] and $BaPb_{1-x}Bi_xO_3$ (x ~ 0.65) [**25**]. In fact, doped BBO showed first time superconductivity with Tc up to ~30 K (high transition temperature) in copper- and iron-free systems [**26**]. It is also predicted theoretically [**20**] that electron doping in BBO can emerge topologically protected surface states (*i.e.*, make it possible topological insulator material).

Apart from crystallographic studies and fundamental transport behavior for these oxide samples, dielectric properties are also very important to get better insight the physical process occurring inside the material. Dielectric properties of non-lead based oxides have received continuous attention for their potential applications in capacitors, actuators, microwave tunable devices (including tunable mixers, filters, and phase shifters) etc. [**11, 27, 28**].

Although Lee *et al.* [**14**] measured temperature dependent loss factor of BBO in the low temperature regime (125 K-250 K) and observed two relaxation peaks at 175 K and 225 K. Still transport properties of BBO in the high temperature regime remain largely unexplored, despite the possibility of numerous interesting applications (e.g. microwave applications, high temperature electrolyte etc.) in this range.

In the present work, BBO sample was synthesized using a solid-state reaction method and its dielectric and impedance spectroscopic characteristics are evaluated in high temperature range (300 K-650 K). To the best of our knowledge, here first time we report existence of two very useful properties (relaxor and negative dielectric constant) in high temperature regime for BBO, which makes it superior from other materials with an extra advantage of using in temperature sensors, thermistors, wave propagation, as electrolyte and bio-membrane functions (due to negative dielectric constant and excellent NTC thermistor characteristic) [**29-32**]. We have also shown through impedance spectroscopy that both grains and grain boundaries contribute in the relaxation process for BBO. Additionally, the quality of the sample is ascertained using detailed investigations of structural, electronic, morphological and chemical properties.

Experimental

Polycrystalline samples of BBO particles were synthesized via standard solid state reaction route using the high purity ($\geq$ 99.9%, Sigma Aldrich) $BaCO_3$ and Bi_2O_3 powders. These powders were weighed according to the stoichiometric formula and ball milled for 48 hours in acetone medium. This mixture was then dried and calcined at 700 °C for 12 h. Calcined powders were then pulverized and mixed with polyvinyl alcohol (PVA) as binder and pressed into pellets of ~10 mm diameter. The pellets were sintered at 750 °C for 12 h. A uniform heating and cooling rate of 2 °C/min was used for both heating and cooling of the furnace.

The crystal structure of the samples was studied using an X-ray diffractometer (Rigaku) employing Cu-Kα (1.54 Å) radiation. Raman spectrum was recorded with micro Raman spectrometer (HORIBA LabRAM HR Evolution) using excitation beam of λ =514.5 nm. Lattice scale imaging with SAED study was accomplished on a high resolution transmission electron microscope (HRTEM Tecnai G20-Stwin 200 kV). Microstructural analysis of the samples was done using a field emission scanning electron microscope (Zeiss EVO 50 SEM). The element distribution/chemical composition was determined by an energy-dispersive X-ray spectrometer (EDS) attached with table-top scanning electron microscope (Hitachi Table Top Microscope TM3000). Further, the dielectric and impedance parameters were obtained over Agilent 4294A Precision Impedance Analyzer.

Results and discussion

Fig. 1 (a) shows the X-ray diffraction pattern obtained on the sample, which confirms that the prepared particles are in single phase. The strong and sharp peaks indicate the crystalline nature of the sample. The diffraction data was

then refined using FullProf program employing the pseudo-voigt profile function **(Fig. 1(a))**.
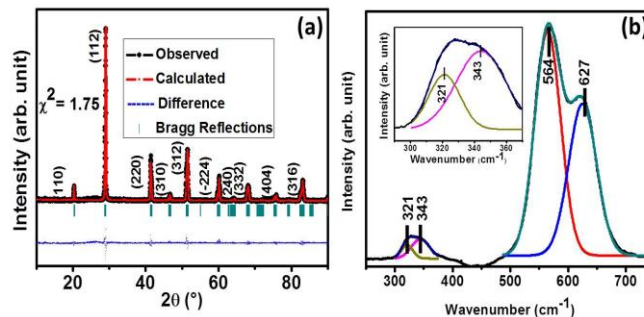
Fig. 1. (a) Observed (black color), calculated (red color), and difference profiles (blue color) with Bragg reflections (olive color) obtained from Rietveld analysis of powder-diffraction pattern of BBO using I2/m space group (b) Raman spectra of BBO, the de-convolution of peak at ~ 327 cm⁻¹ is shown in the inset.

All the diffraction peaks are found to be in accordance with the monoclinic BBO phase having space group I2/m, with the lattice parameters a = 6.18 Å, b = 6.14 Å, c = 8.67 Å, β = 90.17°. These values match well with the JCPDS data card 79-1864 and the basic findings of the Rietveld refinement are tabulated in **Table 1**.

Table 1. Atomic positions for BBO as obtained through Reitveld refinement.

Atomic Level	X	Y	Z	B_{iso} (Å^2)
Ba^{2+}	0.505	0.000	0.248	3.13
Bi^{3+}	0.000	0.000	0.000	1.94
Bi^{5+}	0.000	0.000	0.500	2.24
$O1^{2-}$	0.057	0.000	0.254	1.80
$O2^{2-}$	0.249	0.266	-0.046	1.81
Lattice Parameters	a=6.18 Å	b=6.14 Å	c=8.67 Å	β=90.17°

Raman spectra for BBO sample at room temperature in the frequency range of 250-750 cm⁻¹ is presented in **Fig. 1 (b)**. The Raman spectrum showed two Raman active modes at ~ 327 cm⁻¹ and ~ 567 cm⁻¹. In-depth analysis of these peaks revealed that each of these could be de-convoluted into two peaks. Therefore the de-convolution of these peaks provided four Raman active modes which were located at ~ 321, ~ 343, ~ 564 and ~ 627 cm⁻¹. Strong peaks at ~ 564 cm⁻¹ and ~ 627 cm⁻¹ were corresponding to the out-of-phase breathing mode of a dimerized $BiO_{6/3}$ octahedron [**33**] and triangular pyramidal $BiO_{4/2}$ cluster with localized bipolaron [**34**], respectively. These two different Bi sites (the octahedral $BiO_{6/3}$ and the triangular pyramidal $BiO_{4/2}$ cluster) might originate from some oxygen deficiencies in BBO sample [**34**]. The strong behavior of peak at ~566 cm⁻¹ suggests that the corresponding electron-phonon interaction was closely related to the origin of energy gap generation. On the other hand, the peak at ~ 327 cm⁻¹ had been assigned to the breathing mode coupled with the electron transition from the itinerant state to the local state [**35**]. The peak at ~ 327 cm⁻¹ splits into ~ 321 cm⁻¹ and ~ 343 cm⁻¹ peaks [See Inset **Fig. 1 (b)**], signified that the electronic state of a localized electron got split into two different states corresponding to two different Bi sites, as described above.

The HRTEM micrograph of BBO sample revealed the formation of nearly circular shape nanoparticles of diameter

~ 50-60 nm (see inset (i) **Fig. 2(a)**). The lattice fringe image (**Fig. 2(a)**) exhibits the regular spacing of 0.308 nm, corresponding to the (112) lattice plane of BBO. The ring pattern of SAED (see inset (ii) **Fig. 2(a)**) confirms polycrystalline nature of the prepared sample. SAED pattern marked for different rings; 1: d spacing 0.167 nm (312), 2: d spacing 0.308 nm (112), 3: d spacing 0.39 nm (110); further confirms monoclinic phase of BBO. Thus, the structural parameters obtained from SAED pattern match closely with the XRD results.
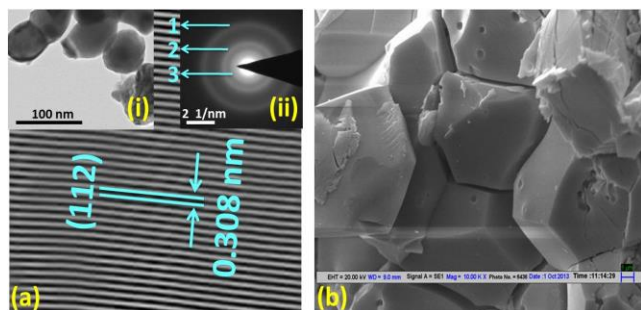
Fig. 2. (a) Lattice scale images of BBO. Inset show (i) low magnification images of nano-particles and (ii) corresponding SAED pattern (b) SEM micrographs of sintered BBO pellet.

The electrical measurements strongly depend on the microstructure and grain growth of the sample. Therefore, to perform such measurements, calcined powder was compressed in the pellet form and sintered at 750 °C for 12 hours. The sintering process results in grain growth and enhancement in particle size. SEM image (**Fig. 2(b)**) of sintered pellet elucidated that sintering treatment lead to the formation of well-defined grains of ~ 15-20 μm size of BBO particles.
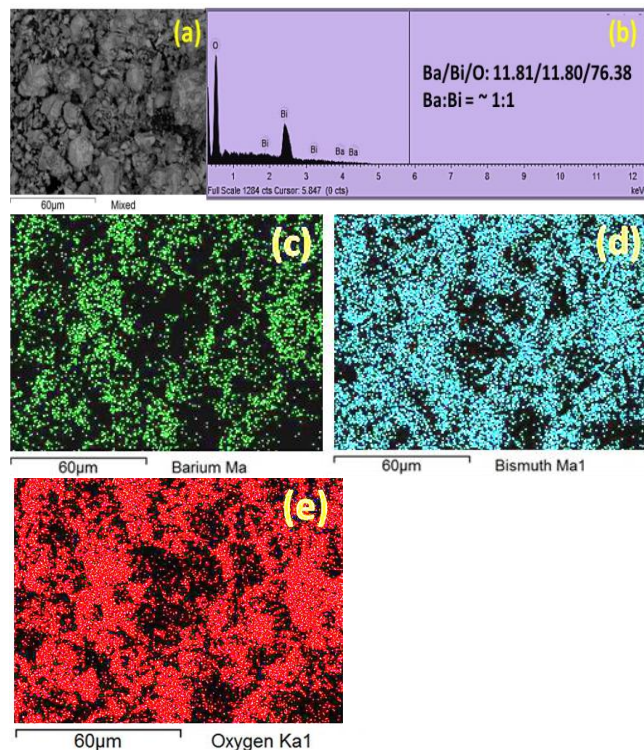
Fig. 3. BBO Particles (a) SEM image (b) EDX spectrum. Elemental mapping of (c) Ba, (d) Bi, and (e) O for BBO particles.

Fig. 3 presents elemental dispersive X-ray spectra (EDS) and elemental mapping of BBO particles. Elements Ba, Bi and O are denoted in green, blue and red in **Fig. 3c**, **3d** and **3e** respectively. These elemental mapping images confirmed the uniform distribution of Ba, Bi and O atoms and showed no particulates of Ba/Bi are taking place, indicating the formation of good quality of the sample. Apart from this, through EDX analysis (**Fig. 3(b)**) the atomic content of Ba/Bi/O was found to be 11.81/11.80/76.38 which clearly depicted the ratio of Ba and Bi as 1:1. The presence of oxygen in environment possibly results into large oxygen content. These results indicate the formation of BBO in desired phase.

Fig. 4 (a) shows the dielectric constant v/s temperature and frequency (see inset) behavior of BBO. In **Fig. 4 (a)**, a pronounced anomaly in the dielectric constant (might originate from monoclinic to rhombohedral transition) shows considerable frequency dependence (peak shifts from ~ 350 K at 10 kHz to ~ 450 K at 1 MHz). A concomitant decrease in the peak value of dielectric constant is also observed. These two features collectively mimic relaxor behavior [36, 37]. The dielectric constant continuously decreases with increasing temperature and bends towards zero. Above 550 K, negative values of dielectric constant are observed. Inset of **Fig. 4 (a)** clearly shows that below 550K, the dielectric constant decreases with increasing frequency. Owing to the electron hopping between Bi^{3+} and Bi^{5+} on the localized sites, at low frequencies (up to ~ 10^4 Hz), the conduction possibly is by hopping of charge carriers that result in the interfacial polarization. However, with increase in frequency, the probability of electrons reaching the grain boundary may decrease, resulting in reduced interfacial polarization. Therefore, the dielectric constant decreases further with increasing frequency up to temperature ~ 500 K. Above this temperature ($\geq$ 550 K), the dielectric constant was found to increase with rise in frequencies and as mentioned above, showed negative values. The materials with negative dielectric constant have attracted great interest among researchers due to their applications in wave propagation, electrolyte behavior, and bio-membrane functions [19]. In order to understand the origin of negative dielectric constant different theories are postulated. Jones *et al*. [38] suggested that relaxation process results in the addition of holes in the material which recombine with free electrons of the dipole and hence reduces the dipole charge leading to negative values of dielectric constant. Champness and Clark [39] claim that the negative values of dielectric constant arise from the inductive behavior of materials [40] and depend on injection of minority carriers. Also, Martens *et al*. [41] proposed a model based on space charge transport and Poisson equation to explain the negative dielectric constant effect, caused by distribution of relaxation times.

The loss factor or dissipation factor, tan δ, (**Fig. 4 (b)**) is an important indicator of a capacitor's quality as it represents the energy loss in a dielectric material. **Fig. 4(b)** showed that the values of tan δ increases with rise in temperature up to ~ 550 K and above this temperature it starts to decrease. The inset of **Fig. 4 (b)** indicates that the dielectric loss factor decreases with increasing frequency and increases with temperature at low frequencies. The

inconsistent lattice vibrations can cause instability in the interfacial polarization which leads to increase in dielectric loss. When the frequency of the external AC field increases and become equal to the hopping frequency of the charge carriers, the maximum electrical energy is transferred to the oscillating ions and creates broad peaks in dielectric loss. A broad peak of tan δ indicates the occurrence of distribution of relaxation time rather than a single relaxation time. When the frequency of applied AC field is much larger than the hopping frequency of electrons, the electrons do not have an opportunity to jump at all and the energy loss is small. In general, the local displacements of electronic charge carriers cause the dielectric polarization in materials. Therefore, the marked decrease in tan δ is due to the decreasing ability of the jumping electrons to follow the alternating frequency of AC electric field beyond certain critical frequency [42]. Overall, it can be concluded that relaxation mechanism in BBO might be the cause behind the negative values of dielectric constant at high temperatures (≥ 550 K).
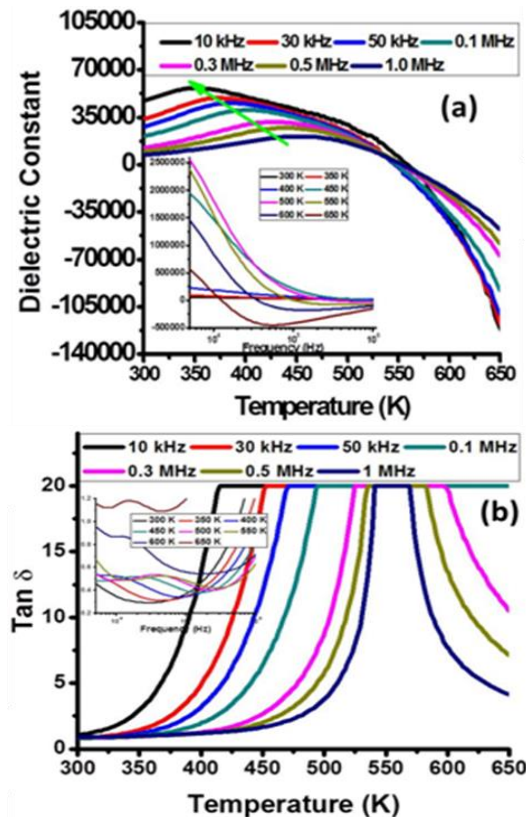
Fig. 4. (a) Dielectric constant (b) dielectric loss vs temperature [and frequency (inset)] behavior of BBO samples.

Fig. 5 (a) shows the variation of real part of impedance (Z', *i.e.,* bulk resistance) with frequency at different temperatures. The Z' value is higher in the low-frequency region and decreases gradually with increasing frequency as a result of increase in ac conductivity ($\sigma_{ac} = \omega\varepsilon_0\varepsilon''$) [43]. The value of Z′ also shows a decreasing trend with increasing temperature [negative temperature coefficient of resistance (NTCR)-type behavior] in the low-frequency region but tends to merge in the high frequency region (≥ 800 kHz) for all temperatures. This behavior at frequencies ≥ 800 kHz indicates the possibility of an increase in ac

conductivity with increase in temperature at higher frequencies; possibly due to the release of space charge as a result of reduction in the grain boundary potential barrier height [44].

The variation of imaginary part of impedance (Z″, *i.e.,* loss spectrum) with frequency at different temperatures is shown in **Fig. 5 (b)**. A significant increase in the broadening of the peaks and shifting of maxima to higher frequency side is observed with rise in temperature, suggested the existence of temperature dependent relaxation phenomenon [45] in BBO particles. Further, the magnitude of Z″ merges in the high frequency region (≥ 800 kHz), provides an indication of the accumulation of space charge in BBO sample, as described above.
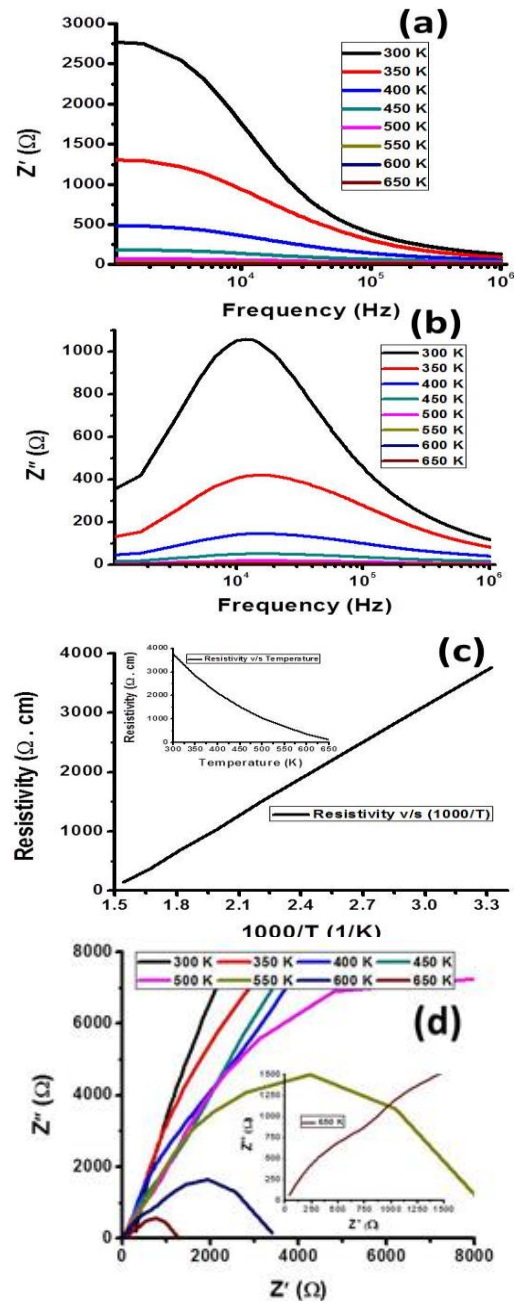
Fig. 5. Variation of (a) real (Z') (b) imaginary part (Z″) of impedance as a function of frequency at different temperatures (c) resistivity v/s (1000/T) curve (Inset shows resistivity v/s temperature behaviour) (d) Nyquist (Z'-Z″) plot at different temperatures (Inset shows zoom view of Nyquist plot at 650K).

Furthermore, the Arrhenius plot (*i.e.*, electrical resistivity v/s 1000/T curve) (**Fig. 5 (c)**) showed straight-line behavior over a wide range of temperatures, indicating an excellent NTC thermistor characteristics for BBO above 550 K. The electrical resistivity versus temperature characteristic (see inset **Fig. 5 (c)**) showed a semiconductor like monotonic decrease of the resistivity with increase of temperature in accordance with the previous report [23].

Fig. 5 (d) shows Nyquist (Z'-Z") plot for BBO sample, at several temperatures. The NTCR behavior in our sample is also validated from this graph. For better clarity, a zoom view of Nyquist (Z'-Z") plot at one representative temperature (650 K) is shown in the inset **Fig. 5 (d)**. The shape of the diagram suggests that the electric response is composed of two semicircles. Thus it can be concluded from the impedance spectroscopy that both grains and grain boundaries contribute to the relaxation process in our sample.

Conclusion

BBO particles were synthesized successfully through solid state technique. XRD and SAED pattern confirmed that BBO particles were crystallized with monoclinic structure in single phase. The electron microscopy revealed that the sintering process results in grain growth which leads to ~ 300-400 times enhancement in particle size. Expectedly, BBO showed semiconducting behavior with resistivity of ~ 3.8 kΩ-cm at room temperature along with an excellent NTC thermistor characteristic above room temperature. The transport studies prove that BBO exhibits two features of practical importance, *i.e.*, relaxor behavior and negative dielectric constant in high temperature regime. Both grains and grain boundaries were found to contribute in the relaxation process from impedance spectroscopy.

Reference

1. Sahoo, S.; Pradhan, D. K.; Choudhary, R. N. P.; Mathur, B. K. *Adv. Mat. Lett.* **2012**, *3*, 97.
   DOI: 10.5185/amlett.2011.4250
2. Tang, X. G.; Chew, K. H.; Chan, H. L. W. *Acta Mater.* **2004**, *52*, 5177.
   DOI: 10.1016/j.actamat.2004.07.028
3. Cross, L. E. *Ferroelectrics*, **1987**, *76*, 241.
   DOI: 10.1080/00150198708016945
4. Zhang, N.; Xu, Z.; Feng, Y.; Yao, X. J. *Electroceram* **2008**, *21*, 609.
   DOI: 10.1007/s10832-007-9249-5
5. Chu, F.; Reaney, I. M.; Setter, N. *J. Appl. Phys.* **1995**, *77*, 1671.
   DOI: 10.1063/1.358856
6. Pati, B.; Choudhary, R. N. P.; Das, P. R.; Parida, B. N.; Padhee, R. *J. Alloy Compd.* **2014**, *6*, 592.
   DOI: 10.1016/j.jallcom.2013.12.241
7. Ray, G.; Sinha, N.; Singh, B.; Bdikin, I.; Kumar, B. *Cryst. Growth Des.* **2015**, *15*, 1852.
   DOI: 10.1021/cg501891r
8. Lin, D.; Kwok, K.W.; Chan, H.L.W. *Ceram. Int.* **2014**, *40*, 6841.
   DOI: 10.1016/j.ceramint.2013.11.147
9. Cheng, S.; Liu, M.; Lu, J.; Lu, L.; Li, L.; Yang, Y. *Ceram. Int.* **2015**, *41*, S319.
   DOI: 10.1016/j.ceramint.2015.03.187
10. Reddy, V. R.; Upadhyay, S. K.; Gupta, A.; Awasthi, A. M.; Hussain, S. *Ceram. Int.* **2014**, *40*, 8333.
    DOI: 10.1016/j.ceramint.2014.01.039
11. Tang, X. G.; Chew, K. H.; Chan, H. L. W. *Acta Mater.*, **2004**, *52*, 5177.
    DOI: 10.1016/j.actamat.2004.07.028
12. Wang, X.; Lu, X.; Zhang, C.; Wu, X.; Cai, W.; Peng, S.; Bo, H.; Kan, Y.; Huang, F.; Zhu, J. *J. Appl. Phys.* **2010**, *107*, 114101.
    DOI: 10.1063/1.3430987
13. Min, K.; Huang, F.; Jin, Y.; Zhu, W.; Zhu, J. *Ferroelectrics*, **2013**, 450, *42*.
    DOI: 10.1080/00150193.2013.838474
14. Lee, S-H; Jung, W-H; Sohn, J-H; Lee, J-H; Cho, S-H *J. Appl. Phys.* **1999**, *86*, 6351.
    DOI: 10.1063/1.371697
15. Mehring, M. *Coord. Chem. Rev.* **2007**, 251, 974.
    DOI: 10.1016/j.ccr.2006.06.005
16. Bazhirov, T.; Coh, S. Louie, S. G.; Cohen, M. L. *Phys. Rev. B* **2013**, *88*, 224509.
    DOI: 10.1103/PhysRevB.88.224509
17. Kennedy, B. J.; Howard, C. J.; Knight, K. S.; Zhang, Z.; Zhou, Q. *Acta Cryst.* **2006**, B62, 537.
    DOI: 10.1107/S0108768106018842
18. Cox, D.E; Sleight, A.W. *Solid State Commun.* **1976**, 19, 969.
    DOI: 10.1016/0038-1098(76)90632-3
19. Schoop, L. M.; Muchler, L.; Felser, C.; Cava, R. J.; *Inorg. Chem.* **2013**, *52*, 5479.
    DOI: 10.1021/ic400381g
20. Yan, B.; Jansen, M.; Felser, C. *Nature Phys.* **2013**, *9*, 709.
    DOI: 10.1038/NPHYS2762
21. Scholder, R.; Ganter, K.-W.; Gläser, H.; Merz, G. *Z Anorg Allg Chem.* **1963**, *319*, 375.
    DOI: 10.1002/zaac.19633190518
22. Namatame, H.; Fujimori, A.; Takagi, H.; Uchida, S.; Groot, F. M. F. D.; Fuggle, J. C.; *Phys. Rev. B* **1993**, *48*, 16917.
    DOI: 10.1103/PhysRevB.48.16917
23. Luo, Y; Li, X.; Liu, X. *Adv. Mater. Sci. Eng.* **2009**, 2009, 1.
    DOI: 10.1155/2009/383842
24. Mattheiss, L. F.; Gyorgy, E. M.; Johnson, D. W. *Phys. Rev. B* **1988**, *37*, 3745.
    DOI: 10.1103/PhysRevB.37.3745
25. Sleight, A.; Gillson, J.; Bierstedt, P. *Solid State Commun.* **1975**, 17, 27.
    DOI: 10.1016/0038-1098(75)90327-0
26. Li, G.; Yan, B.; Thomale, R.; Hanke, W. *Sci. Rep.* **2015**, *5*, 10435.
    DOI: 10.1038/srep10435
27. Zhang, M.; Zhai, J.; Shen, B.; Yao, X. *J. Mater. Res.* **2012**, *27*, 910.
    DOI: 10.1557/jmr.2011.429
28. Guerra, J. D. L. S.; Eiras, J. *A. Mat. Res.* **2004**, 7, 325.
    DOI: 10.1590/S1516-14392004000200017
29. Feteira, A. J. *Am. Ceram. Soc.* **2009**, *92*, 967.
    DOI: 10.1111/j.1551-2916.2009.02990.x
30. Jin, H. S.; Yang, C. S.; Lee, J. H.; Park, C. G. *U.S. Patent* 0063401 A1, **2015**.
31. Chu, C. W.; Chen, F.; Shulman, J.; Tsui, S.; Xue, Y. Y.; Wen, W.; Sheng, *P. Proc. SPIE* **2005**, 5932, 59320X.
    DOI: 10.1117/12.626267
32. Chu, C. W.; Chen, F.; Xue, Y. Y.; Shulman, J.; Tsui, S. *U.S. Patent* 7611969 B2, **2009**.
33. Sugai, S. *Solid State Commun.* **1989**, 72, 1187.
    DOI: 10.1016/0038-1098(89)90792-8
34. Kambe, S.; Shime, I.; Ohshima, S.; Okuyama, K., Sakamoto, K. *Solid State Ionics* **1998**, 108, 307.
    DOI: 10.1016/S0167-2738(98)00055-1
35. Sugai, S. *Phys. Rev. B* **1987**, *35*, 3621.
    DOI: 10.1103/PhysRevB.35.3621
36. Singh, A.; Panday, V.; Kotnala, R.K.; Panday, D. *Phys. Rev. Lett.* **2008**, *101*, 247602.
    DOI: 10.1103/PhysRevLett.101.247602
37. Bhattacharjee, S.; Panday, V.; Kotnala, R. K.; Panday, D. *Appl. Phys. Lett.* **2009**, *94*, 012906.
    DOI: 10.1063/1.3068000
38. Jones, B. K.; Santana, J.; McPherson, M. *Solid State Commun.* **1998**, *107*, 47.
    DOI: 10.1016/S0038-1098(98)00162-8
39. Champness, C. H.; Clark, W. R. *Appl. Phys. Lett.* **1990**, *56*, 1104.
    DOI: 10.1063/1.102581
40. Gordon, K. L.; Kang, J. H.; Park, C.; Lillehei, P. T.; Harrison, J. S. *J. Appl. Polym. Sci.* **2012**, 125, 2977.

DOI: 10.1002/app.36248

41. Martens, H. C. F.; Huiberts, J. N.; Blom, P. W. M. *Appl. Phys. Lett*. **2000**, 77, 1852.
    DOI: 10.1063/1.1311599

42. Hassan, R.; Hassan, J.; Hashim, M.; Paiman, S.; Azis, R. S. *Journal of Advanced Ceramics* **2014**, *3*, 306.
    DOI: 10.1007/s40145-014-0122-0

43. Singh, A. P.; Gupta, B. K.; Mishra, M.; Govind; Chandra, A.; Mathur, R.B.; Dhawan, S. K. *Carbon*, **2013**, *56*, 86.
    DOI: 10.1016/j.carbon.2012.12.081

44. Suman, C. K.; Prasad, K.; Choudhary, R. N. P.; J. *Mater. Sci* **2006**, 41, 369-375.
    DOI: 10.1007/s10853-005-2620-5

45. Behera, S.; Das, P. R.; Parida, B. N.; Nayak, P.; Choudhary, R. N. P. *Adv. Mat. Lett.* **2014**, *5*, 143-147.
    DOI: 10.5185/amlett.2013.fdm.60